

RESEARCH ARTICLE

10.1002/2015JC011276

Key Points:

- Infrared (IR) images clearly separate active and residual lifetime stages of whitecaps
- First quantifications of whitecap lifetime stages from IR images
- Whitecap signatures in IR images allow detection of whitecaps in radiometric measurements

Correspondence to:

H. Potter,
henry.potter.ctr@nrl.navy.mil

Citation:

Potter, H., G. B. Smith, C. M. Snow, D. J. Dowgiallo, J. P. Bobak, and M. D. Angelova (2015), Whitecap lifetime stages from infrared imagery with implications for microwave radiometric measurements of whitecap fraction, *J. Geophys. Res. Oceans*, 120, 7521–7537, doi:10.1002/2015JC011276.

Received 27 AUG 2015

Accepted 20 OCT 2015

Accepted article online 29 OCT 2015

Published online 20 NOV 2015

Whitecap lifetime stages from infrared imagery with implications for microwave radiometric measurements of whitecap fraction

Henry Potter¹, Geoffrey B. Smith¹, Charlotte M. Snow², David J. Dowgiallo¹, Justin P. Bobak¹, and Magdalena D. Angelova¹

¹Remote Sensing Division, Naval Research Laboratory, Washington, District of Columbia, USA, ²Marine Geosciences Division, Naval Research Laboratory, Stennis Space Center, Mississippi, USA

Abstract Quantifying active and residual whitecap fractions separately can improve parameterizations of air-sea fluxes associated with breaking waves. We use data from a multi-instrumental field campaign on Floating Instrument Platform (FLIP) to simultaneously capture the signatures of active and residual whitecaps at visible, infrared (IR), and microwave wavelengths using, respectively, video camera, mid-IR camera, and a radiometer at 10 GHz. We present results from processing and analyzing IR images and correlating this information with radiometric time series of brightness temperature at horizontal and vertical polarizations T_{BH} and T_{BV} . The results provide evidence that breaking crests and decaying foam appear in mid-IR as bright and dark pixels clearly distinguishing active from residual whitecaps. We quantify the durations of whitecap lifetime stages from the IR images and identify their corresponding signatures in T_B time series. Results show that T_{BH} and T_{BV} vary in phase during the active and in antiphase during the residual whitecap stages. A methodology to distinguish active and residual whitecaps in radiometric time series without a priori IR information has been developed and verified with corresponding IR and video images. The method uses the degree of polarization P (the ratio between the sum and difference of T_{BV} and T_{BH}) to capture whitecaps as prominent spikes. The maximum and zero-crossing of the first derivative of P serve to identify the presence of active whitecaps, while the minimum of dP marks the transition from active to residual whitecap stage. The findings have implications for radiometric measurements of active and total whitecap fractions.

1. Introduction

Oceanic whitecaps are fleeting, transient features on the ocean surface manifesting the highly intermittent process of breaking of wind waves with air entrainment. The whitecaps are dynamic entities that evolve quickly. Their formation and growth are on a time scale of one third of the wave period, while their decay lasts for one to several wave periods depending on the wind speed and the environmental conditions such as water temperature, salinity, and surfactants [Monahan *et al.*, 1982; Angelova and Huq, 2012; Callaghan *et al.*, 2012]. Though the whitecap evolution is a continuous process, we often try to separate the whitecap lifetime into two stages because each stage has distinct physical characteristics and is associated with different air-sea interaction (ASI) processes [Paget *et al.*, 2015]. We denote these two stages as active (also known as young or stage A) and residual (also known as mature or stage B) whitecaps [Monahan and Woolf, 1989] and quantify them with whitecap fractions W_A and W_B , respectively. Such separation affords the parameterization of surface fluxes of momentum, heat, and mass in terms of the most suitable quantity W_A , W_B , or the total whitecap fraction $W = W_A + W_B$.

Whitecap fraction W has been measured extensively because it is a direct expression of wave breaking and thus a suitable forcing variable for myriad ASI processes; summaries of whitecap data sets are given by Monahan and O'Muircheartaigh [1986], Angelova and Webster [2006], and de Leeuw *et al.* [2011]. The photographic method, based on image intensity thresholding I , has been the workhorse of measuring whitecap fraction $W(I)$ for decades. Data sets providing specifically $W_A(I)$ or $W_B(I)$ are much fewer; Table 1 in M. D. Angelova and P. A. Hwang (Using energy dissipation rate to obtain active whitecap fraction, submitted to *Journal of Physical Oceanography*, 2015) lists only 13 data sets for $W_A(I)$ gathered since 1971. The separation

of active and residual whitecaps in sea state photographs is not easy because of the continuous and subtle change of the image intensity from the active to the residual stage. Algorithms that find the most suitable intensity threshold by analyzing the image intensity have improved this separation in recent years [Sugihara *et al.*, 2007; Callaghan and White, 2009; Bobak *et al.*, 2011; Scanlon and Ward, 2013]. The use of the kinematic properties of the whitecaps—such as whitecap motion (i.e., speed and direction)—in addition to the intensity thresholding ensures more objective separation of the active whitecap fraction W_A [Mironov and Dulov, 2008; Kleiss and Melville, 2010, 2011].

Increasingly available data for energy dissipation rate ε from direct in situ measurements [e.g., Gemmrich *et al.*, 2008] or from measured or modeled wave spectra [e.g., Hanson and Phillips, 1999] or from wave models [e.g., Rogers *et al.*, 2012] offer an alternative method of estimating active and total whitecap fractions using empirical or analytical expressions $W_A(\varepsilon)$ or $W(\varepsilon)$ [e.g., Hanson and Phillips, 1999]. Anguelova and Hwang (submitted manuscript, 2015) have demonstrated that an expression $W_A(\varepsilon)$ derived on the basis of Phillips [1985] concept of breaking crest length distribution can be combined with buoy data for wave spectra to produce $W_A(\varepsilon)$ values comparable to those obtained from photographic measurements $W_A(l)$.

Satellite-based radiometric observations of the ocean surface brightness temperature T_B at microwave frequencies (1–37 GHz) afford another independent method for estimating whitecap fraction $W(T_B)$ [Anguelova and Webster, 2006; Anguelova *et al.*, 2006, 2009]. The availability of $W(T_B)$ data on a global scale over long periods provide consistent database of whitecap fraction and additional meteorological and oceanographic variables covering a wide range of conditions. A yearlong database $W(T_B)$ with six additional variables [Anguelova *et al.*, 2010] has proven useful so far to investigate the variability of whitecap fraction [Salisbury *et al.*, 2013, 2014].

By virtue of its measuring principle, passive microwave observations of T_B provide the total whitecap fraction W [Anguelova and Gaiser, 2011]. However, to more fully use such a database for parameterizations and studies of dynamic processes in the upper ocean, we need to find a way to extract W_A from $W(T_B)$. One approach is to match in time and space satellite-based $W(T_B)$ data with objectively determined in situ data $W_A(\varepsilon)$ or $W_A(l)$ (e.g., Anguelova and Hwang, submitted manuscript, 2015) and develop a scaling factor $R = W_A/W$. Preliminary results on combining $W(T_B)$ from satellite and $W_A(\varepsilon)$ from buoys have been presented [Anguelova and Hwang, 2012]. This scaling factor can be generalized to be applicable beyond the matched satellite-in situ pairs by parameterizing it in terms of readily measured variables (e.g., wind speed at 10 m reference height U_{10} or latitude). Use of such a scaling factor with newly available satellite T_B data will provide both W and W_A from radiometric measurements.

Another approach to extract W_A from $W(T_B)$ is to be able to differentiate the T_B data which provide either W or W_A . The effect of individual whitecaps is seen in time series of T_B at horizontal and vertical (H and V) polarizations (hereafter referred to as T_{BH} and T_{BV}) as sharp spikes with varying amplitudes [Nordberg *et al.*, 1971; Wang *et al.*, 1995; Padmanabhan *et al.*, 2006]. The root cause for observing T_{BH} and T_{BV} peaks in presence of whitecaps is the high, black-body-like emissivity of the sea foam. Two closely linked components ensure high foam emissivity, namely high absorption losses in a coupled foam-seawater system and effective transmission of electromagnetic (EM) radiation into and through the foam resulting from impedance matching of the radiation properties of the air and seawater [Williams, 1971; Anguelova and Gaiser, 2012].

As for the variability of the T_B spikes, there are different reasons for the varying amplitudes of these spikes between H and V polarizations, as well as within each polarization. The key element for the variability from a measuring viewpoint is nonuniform beam filling, i.e., how much of the radiometer beam is occupied by the breaker. One reason for the variability from physical viewpoint is the wide range of wave scales [Gemmrich *et al.*, 2008] which could produce spikes either because waves break with whitecap formation or because waves are steep [Jessup *et al.*, 1990]. Such cases introduce some ambiguity when associating T_{BH} and T_{BV} spikes with whitecaps. This ambiguity could be resolved using the fact that changes of T_B due to rough sea and steep waves depend on the polarization of the EM radiation [Hollinger, 1971], while changes of T_B due to whitecaps are polarization independent [Rose *et al.*, 2002]. That is, because foam depolarizes the EM radiation [Anguelova and Gaiser, 2013], spikes due to whitecaps must be observed simultaneously at both H and V polarizations [Smith, 1988; Padmanabhan *et al.*, 2006].

Another physical reason for spikes with different amplitudes in T_{BH} and T_{BV} time series is that active and residual whitecaps have different emissivity. Similar to the case of image intensity in photographs of the

sea state, the differences in the foam emissivity due to thick and bright active whitecaps or thin and dim residual whitecaps are small and subtle [see *Anguelova and Gaiser*, 2011, Table 3]. One needs additional information to recognize and separate T_B values caused by active or residual foam. Video records taken simultaneously with microwave observations is one approach that has been used [*Smith*, 1988; *Padmanabhan et al.*, 2006; *Catalán et al.*, 2011]. However, infrared (IR) imagery can provide more objective separation of the active and residual lifetime stages of whitecaps.

Foam within the whitecaps is highly reflective in the visible portion of the EM spectrum (wavelengths from 400 to 750 nm) with reflectance r up to 60% from thick foam layers [*Whitlock et al.*, 1982]. The foam reflectance r noticeably decreases in the near and medium IR region (wavelengths up to 4 μm) due to increasing absorption by seawater content of foam, and reaches values $r \leq 10\%$ [*Whitlock et al.*, 1982; *Koepke*, 1984; *Frouin et al.*, 1996; *Kokhanovsky*, 2004]. In the far (thermal) IR portion of the EM spectrum (wavelengths 8–14 μm), foam is highly emissive with emissivity e close to unity [*Niclòs et al.*, 2007]; this is similar to the high foam emissivity at microwave frequencies [*Anguelova and Gaiser*, 2012]. With such wide differences of the signals at different wavelengths, foam has specific remote sensing signatures at different portions of the EM spectrum [*Koepke*, 1986; *Jessup et al.*, 1997a; *Williams*, 1971]. However, between the extrema of high foam reflectivity at visible wavelengths and the high foam emissivity at microwave frequencies, the foam signal in the IR portion of the EM spectrum shows a dichotomy which can overcome the difficulties arising from the small variations in the visible r and in the microwave e . *Jessup et al.* [1997a] first reported on the specific signature of breaking waves at IR wavelengths. They showed direct link between the thermal disruption and recovery of the surface skin layer to the energy loss by wave breaking. This opened the possibility to study not only breakers [*Carini et al.*, 2015] but also microscale wave breaking (without air entrainment) [*Jessup et al.*, 1997b; *Sutherland and Melville*, 2013] as well as its contribution to air-water gas transfer [*Zappa et al.*, 2001] and near-surface turbulence [*Sutherland and Melville*, 2015]. The study reported here builds on the serendipitous observations from airborne IR imagery by *Marmorino and Smith* [2005] that whitecaps on actively breaking wave crests appear relatively bright, while residual whitecaps appear dark compared to the ambient water. This dichotomic signal from foam in IR imagery can inform us on separating active and residual whitecaps observed as different changes of T_B data.

To this end, we conducted the Breaking Wave Experiment (BREWEX) on board the Floating Instrument Platform (FLIP) from 17 April 2012 to 3 May 2012 (Year Days (YD) 108–124) [*Anguelova et al.*, 2013]. BREWEX was a multi-instrument field campaign with the overall goal of observing, identifying, and correlating the signatures of active and residual whitecaps using visible, infrared, microwave, and acoustic data. *Savelyev et al.* [2014] presented the first results of the BREWEX data analysis focusing on the relationship between sea spray aerosol production and brightness temperature of breaking waves. The focus of this study is analysis and correlation of the IR images and the radiometric data collected during BREWEX. The study objectives are to: (1) verify the bright-dark signature of active and residual whitecaps in IR imagery; (2) quantify whitecap lifetimes from IR images; (3) use this information to identify breaking events in time series of radiometric data T_B ; (4) assess the utility of the whitecap IR signature to distinguish whitecap lifetime stages in T_B data.

2. Instrumentation

FLIP is a unique research vessel that provides a stable platform for near-surface and underwater measurements (<http://www-mpl.ucsd.edu/resources/flip.intro.html>). FLIP was towed north from San Diego to approximately 150 km west from Monterey Bay (red line in Figure 1a). It was flipped into vertical position at that location on 21 April (YD 112) and was left to drift with the wind and ocean currents. Data were collected from FLIP's port and starboard booms (each ~ 18 m long) from 22 to 30 April (YD 113–121) along a track generally due south (cyan line in Figures 1a and 1b). Water depth of ~ 3000 m provided deep water breaking conditions, which are suitable for comparisons to satellite-based passive microwave observations from radiometers like WindSat [*Gaiser et al.*, 2004].

2.1. Radiometric Observations

Observations of brightness temperature of the ocean surface T_B were made with two microwave radiometers operating at 10.7 and 37 GHz, V and H polarizations. The radiometers are a subset of the Airborne Polarimetric Microwave Imaging Radiometer (APMIR) built at Naval Research Laboratory [*Bobak et al.*, 2001,

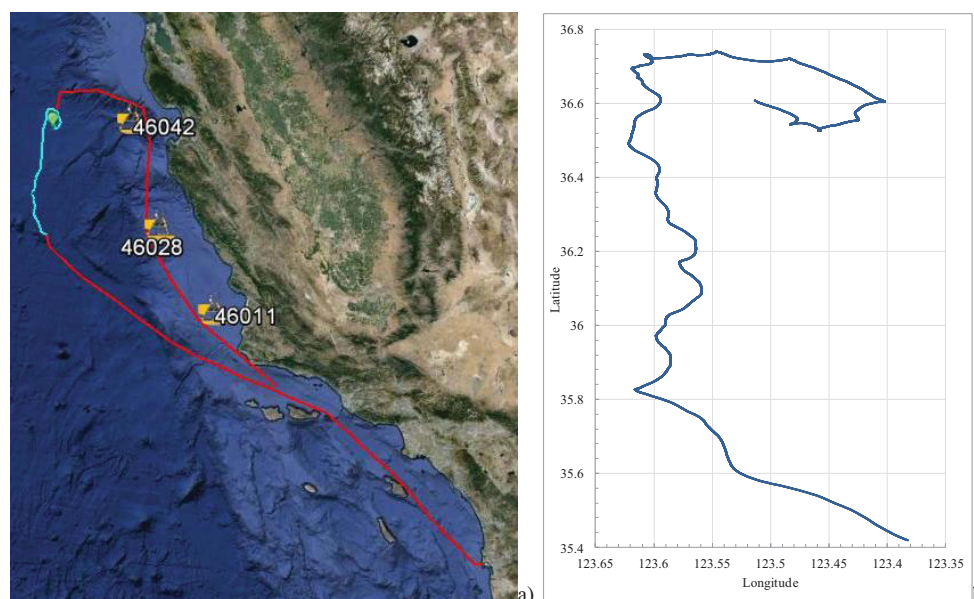


Figure 1. Field experiment location: (a) towing FLIP to destination and close by buoys and (b) close view of FLIP trajectory while drifting south along the California coast.

2011]. The T_b time series at 10.7 GHz synchronized to Coordinated Universal Time (UTC) are used in this study. The radiometers were enclosed in a weather casing with a window viewing the scene through a low-loss dielectric cover (Cuming Microwave PF3). The radiometer enclosure was mounted on the port boom 11.18 m from FLIP's hull (white box in Figure 2a). At this position on the boom, the observed breaking wave field was downwind and resulted from unperturbed airflow. The 10 GHz radiometer was 12.54 m above the mean water level (MWL) looking at the surface at incidence angle of 45.2° from nadir. This setup yielded an elliptical footprint of approximately 2.61 m by 1.83 m with the long axis in the radiometer line of sight (Figure 2b).

End-to-end calibration of the radiometers was provided by rotating the enclosure to left and right to look at two external targets mounted on the port boom. The cold target was a metal sheet reflecting sky radiation (seen in Figure 2a), and the warm target was microwave absorbing material at ambient air temperature. Both targets were protected with low-loss dielectric covers. Internal calibration allowed correcting for the radiometer's thermal gain drift during intervals between the external, end-to-end calibrations. The internal calibration was provided by noise diodes and ambient terminations.

A video camera (1/3" mid-res, EverFocus) was installed together with the radiometers inside the weather casing. The camera was positioned 12.15 m above the MWL with the same incidence angle of 45.2° as the 10 GHz radiometer. The imaged (rectangular) area on the water surface was rectified for the oblique look angle to a trapezoid. With camera focus length and zoom adjustment, the trapezoid field of view (FOV) of the video sensor had a length of 1.43 m along the line of sight; the near, center, and far side horizontal dimensions were 1.86, 2.15, and 2.59 m, respectively (Figure 2b). Video images were recorded at 10 frames per second (fps) (every 100 ms).

2.2. Infrared Imagery

The IR camera was mounted on top of the radiometers (black weather casing in Figure 2a) to ensure the radiometer footprints fell within the FOV of the IR camera (Figure 2b). The IR sensor (Merlin Mid, Indigo, Inc.) was responsive to 3–5 μm radiation (midwave IR), had a temperature sensitivity of about 0.02 K, and an array size of 320×256 pixels. It was equipped with a 13 mm lens that provided an FOV with horizontal θ_h and vertical θ_v viewing angles of 40.5° and 32.9° , respectively. The sensor was 13.29 m above the MWL and pointed 43.2° from nadir. This resulted in a (rectified) trapezoid surface area of $\sim 345 \text{ m}^2$ with approximately 16 m in length along the line of sight with the widths of 11 m nearside, 13.5 m center, and 19.4 m far side

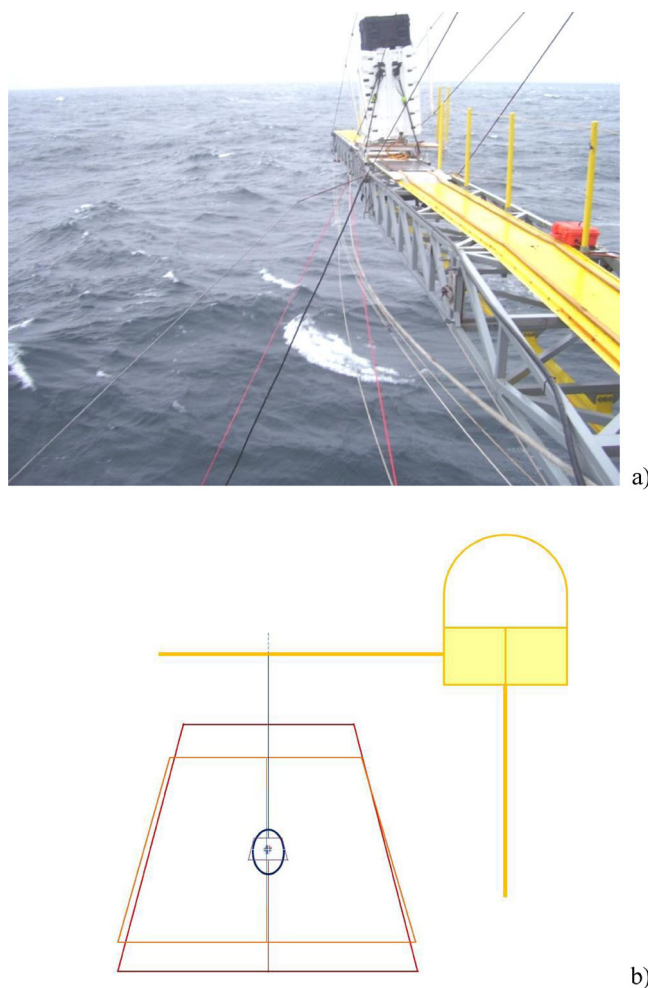


Figure 2. Field deployment: (a) radiometers at 10 and 37 GHz (white casing) and infrared (IR) camera (black casing) on FLIP port board. Each casing also includes video camera; (b) instrument fields of views: IR camera (red), accompanying video camera (yellow), 10 GHz radiometer (blue ellipse), and accompanying video camera (purple).

(Figure 2b). This geometry yields a 4.2 cm spatial resolution at center, 3.4 cm nearside, and 6.1 cm far side. Imagery was recorded at sampling rate of 60 Hz.

A visible monochromatic camera was installed atop the IR camera in the same (black) weather casing. The visible sensor (SI-1920HD, Silicon Imaging) had an array size of 1920×1080 pixels. It was equipped with a 12 mm lens that provided an FOV of $\theta_h = 43.6^\circ$ and $\theta_v = 25.4^\circ$. Its position was 13.39 m above the MWL, with a horizontal distance from the center of the IR camera of 9 cm. It pointed 43.2° from nadir, the same as the IR camera. The rectified imaged area was a trapezoid with an area of $\sim 378 \text{ m}^2$, of length 11.9 m, and widths 12.4 m nearside, 14.7 m at center, and 19.1 m far side (Figure 2b). This geometric setting yielded a spatial resolution 0.65 cm nearside, 0.77 cm at center, and 1 cm far side. Imagery was recorded at 20 Hz.

Data from both sensors was stored to a DVR (DVR Express Core, IO Industries) which captured the full frame rate data from each camera asynchronously, time stamping each frame independently. Times were synchronized to UTC via a feed from a GPS receiver (GS-101 GPS Synchronized Time Code Generator, Orca Technologies). An error in the Time Code Generator occurred during the deployment

that necessitated reconstruction of some of the timing information during postprocessing and resulted in uncertainty in the time stamps $\sigma_{\text{IR}} = \pm 0.52 \text{ s}$.

2.3. Experimental Conditions

Six weather parameters (wind speed, wind direction, air temperature, relative humidity, barometric pressure, and precipitation) were monitored with a meteorological station (Vaisala WXT520 Weather Transmitter) mounted at the end of the starboard boom 10 m above the MWL. The sampling rate was every 5 s. The wind speed during BREWEX was in the $2.8\text{--}18 \text{ m s}^{-1}$ range. Figure 3 shows the wind speed for YDs 119–120 when most breaking events were recorded; each point in the figure represents average of U_{10} values for 20 min interval.

A pressure sensor attached to the starboard boom at 5 m depth was used to collect data for obtaining surface wave spectra and wave field characteristics. The pressure signal was sampled at 10 Hz. For YDs 119–120, significant wave heights from 3 to $\sim 5 \text{ m}$ were measured [Anguelova *et al.*, 2013] with the spectral peak periods of the wind-sea and swell components ranging from ~ 8 to 13 s [Hwang *et al.*, 2015] and wind-sea peak phase speed ranging from 8 to $\sim 15 \text{ m s}^{-1}$. The environmental conditions during BREWEX were sea-water temperature of 13°C in the mixed layer (0–10 m), nearly neutral atmospheric stability, and salinity of 32.6 practical salinity unit (psu) [Saveljev *et al.*, 2014].

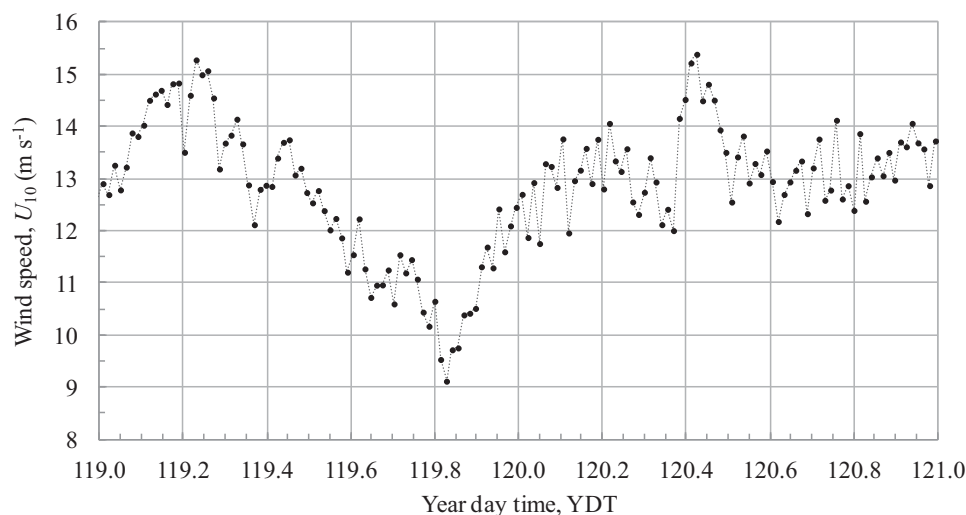


Figure 3. Wind speed conditions for 28 and 29 April 2012 (Julian days 119 and 120) when the IR imagery and brightness temperature time series analyzed in this study are collected.

3. Data Collection and Processing

3.1. Radiometric Data

Radiometric brightness temperature T_B data were stored in intervals of approximately 20 min. A total of 60 20 min data runs (i.e., 20 h) of data were recorded. Most 20 min data runs are for the high wind speed conditions during YDs 119–120 (Figure 3). During each 20 min interval, the data were collected continuously at a sampling rate of 20 Hz alternating between the scene and the internal calibration load (section 2.1). Figure 4 shows typical time series of T_B at H and V polarizations (T_{BH} and T_{BV}). The 20 min time series in Figure 4a exemplifies T_B variations caused by sea surface roughness at low winds ($U_{10} = 3.6 \text{ m s}^{-1}$) on YD 115. Averaged T_B values are monotonic over the entire period with variations of T_{BH} ranging from 81 to 100 K and variations of T_{BV} from 130 to 161 K. The 20 min time series in Figure 4b show T_B data for breaking waves at $U_{10} = 11.9 \text{ m s}^{-1}$ on YD 119. The presence of whitecaps does not change the mean T_B values significantly; e.g., mean values of T_{BH} and T_{BV} for different time series change from less than 1% to at most $\sim 4\%$. However, the variability increased substantially; e.g., for Figure 4, the standard deviations of the T_{BH} and T_{BV} time series increased by a factor of ~ 2 . Many spikes in the time series in Figure 4b are another prominent feature, reaching a maximum of 128 K for T_{BH} and 176 K for T_{BV} . Figure 5 zooms in on 5 min of the T_B time series in Figure 4b to clearly show the spikes. The red vertical lines show cases when there are spikes at both H and V polarizations; the blue vertical lines show cases when there are pronounced spikes in only H or V. Following previous observations (section 1), the former should be associated with whitecaps from breaking waves, while the latter could signify steep, but not breaking waves. The question that arises: can we use such T_B time series to identify breaking events and to distinguish different stages of the whitecap lifetimes? To answer this question, we can analyze the T_{BH} and T_{BV} in tandem (like in Figure 5a), or look at different combinations of the two polarizations, e.g., their sum, difference, ratio, etc. (denoted in Figure 5b as $V + H$, $V - H$, and H/V , respectively). The same vertical lines (red and blue) show pronounced and similar maxima in the $V + H$ time series for all cases marked in Figure 5a. The same cases show up as strong minima in the $V - H$ time series and as spikes close to unity in the H/V time series. Figure 5b thus clearly demonstrates the ambiguity in identifying breaking events using the T_B values alone. One needs additional information to verify the information given by the T_B values. Previous observations (section 1) suggest that IR imagery can provide unambiguous identification of both breaking events and their lifetime stages. By establishing unambiguous criterion for whitecaps presence and lifetime stages in T_B time series using IR imagery, we will be able to apply it to new, independent T_B time series to distinguish whitecaps and their active and residual lifetime stages.

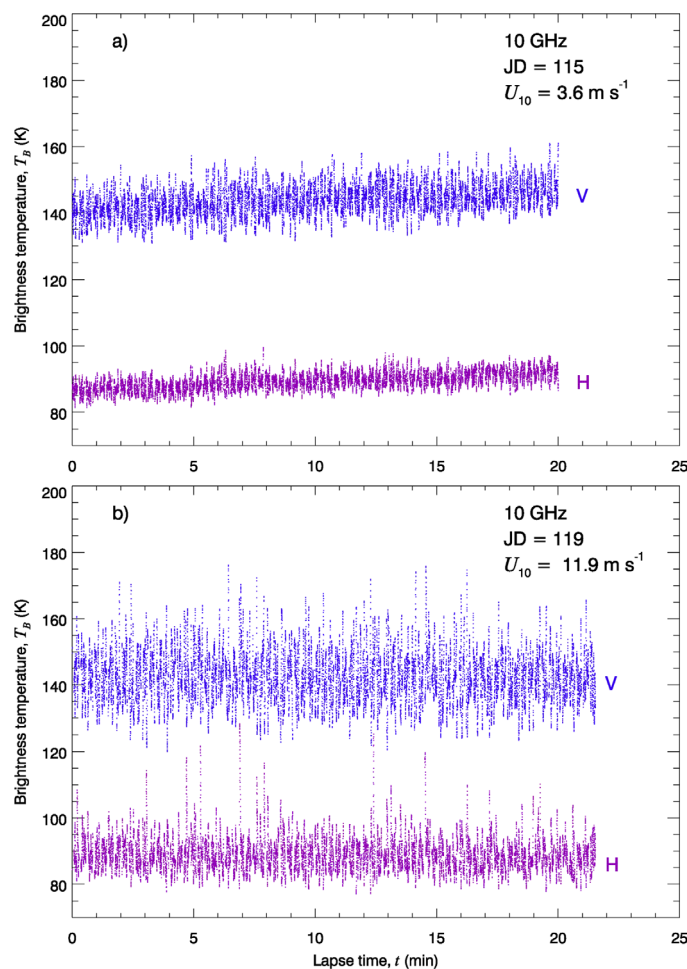


Figure 4. Time series (of ~ 20 min) of brightness temperature T_B at horizontal (H, purple) and vertical (V, blue) polarizations: (a) for rough sea surface without whitecaps (low wind speed) and (b) for breaking waves and whitecaps (high wind speed).

defined for each breaking event. This was done to isolate the breaking event from any image anomalies, such as edge effects, foam from previous breaking events, or glint. Once defined, the ROI used to calculate the fractional coverage for each event remained constant. The areas of the ROIs compare more closely to the radiometer footprint than to full IR FOV (Figure 2b). Next, two thresholds were applied to each image: a threshold of high image intensity which isolated the bright pixel representing the active whitecaps, and a threshold with low intensity which isolated the dark pixel representing the residual whitecaps. Thresholds were determined subjectively for each breaking event in order to capture the whitecap lifetime stages while avoiding inclusion of background features such as glint. Because each event was acquired under unique conditions (e.g., breaking direction, location within ROI, and sun angle), use of invariant thresholds for different breaking events was not viable. However, thresholds remained fixed for all images during each individual breaking event.

The thresholded areas thus extracted were then used to quantify the temporal evolution of the active and residual whitecaps. For every fifth frame (12 Hz) throughout the breaking event, the number of pixels above (below) the bright (dark) threshold was summed to provide the relative contribution of active (residual) whitecaps to the area within the ROI. The number of bright and dark pixels in each frame was normalized by their respective event maxima. An example of the outcome of this processing procedure for the event in Figure 6 is shown in Figure 7. The horizontal axis is time in seconds, with an arbitrary start. The vertical axis shows normalized relative area for the active whitecap (green) and the residual whitecap (red). The notations (a), (b), and (c) correspond to the images in Figure 6. Image (a) is during the peak of

3.2. Infrared Images

Infrared images were typically collected nearly continuously for several hours after which a break would be taken for download and backup of the data. For ease of postprocessing, the image records were broken into segments, each approximately 3 min long. Each 3 min run was manually examined for suitable breaking events. Image quality, contrast, and glint are the parameters used to decide if a breaking event was suitable for analysis. Figure 6 shows typical example of an identified breaking event, visible images on top and IR below. Image pairs (a), (b), and (c) were captured at 2, 6.5, and 8.5 s from the onset of the breaking. In the visible images, active and residual foam are both bright compared with the background. In the infrared images, the regions of active (residual) foam are distinctly brighter (darker) than the surface.

IR images like those in Figure 6 were used to obtain the areal fraction of the whitecaps in their active and residual stages. First, a region of interest (ROI) was

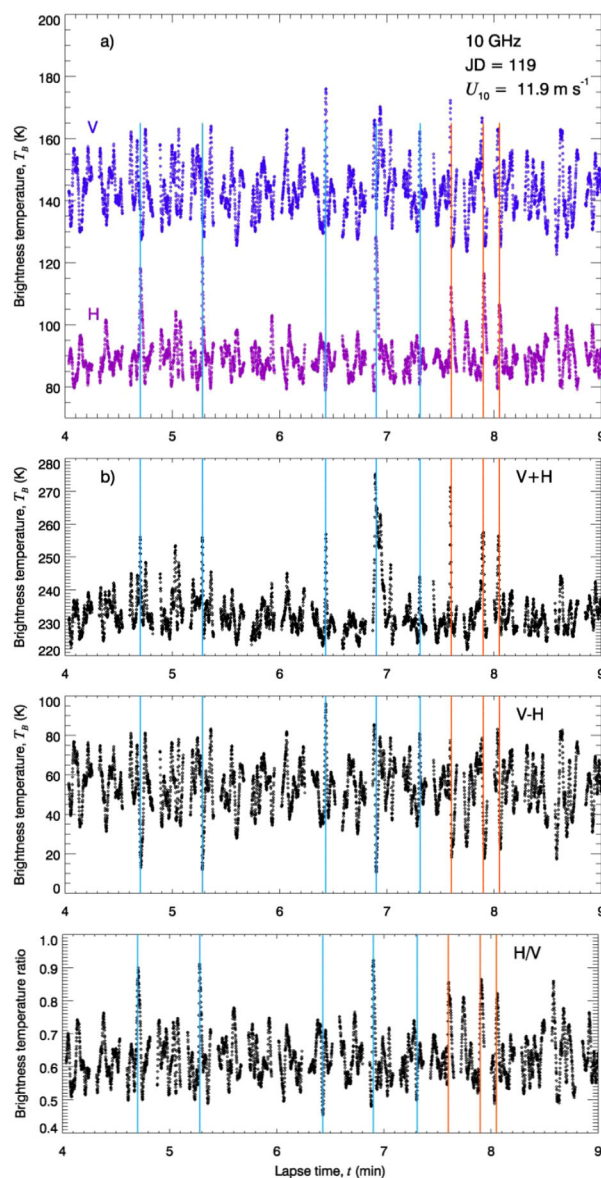


Figure 5. Time series of T_B for high wind speed: (a) zoom-in on 5 min of T_B in Figure 4b; (b) sum, difference, and ratio of T_B at H and V polarizations. Red vertical lines show simultaneous peaks in both T_{BH} and T_{BV} ; blue vertical lines show peaks in either of the polarizations.

with two or more distinctive peaks, such as that shown in Figure 8c. Laboratory observations of bubble clouds have documented multiple decaying plumes in the trough of the wave profile [Anguelova and Huq, 2012, their Figures 8–10]. This suggests that the observed secondary and subsequent peaks in Figures 7 and 8 are possibly due to subsurface bubble plumes rising to the surface to replenish decayed surface bubbles.

Bright areas grow to a maximum value for ~ 1 s, a time consistent with that observed in field and laboratory experiments from video images [Callaghan *et al.*, 2012, 2013]. The active stage duration τ_A ranges from 0.4 to 5 s. The residual foam had lifetime τ_B which ranged from about 3–30 s. These decay times are much longer than those observed by Callaghan *et al.* [2012] from video images in the field (up to 6 s) under comparable wind speeds ($8\text{--}13\text{ m s}^{-1}$). Such differences could be expected because faint decaying bubbles are less effectively captured in video than in IR imagery. Different water properties (sea surface temperature, salinity, surfactants) may also contribute to this difference. The duration of the residual stage τ_B was up to 10 times longer than the active stage duration τ_A . However, in some cases, the ROI did not capture the entire

the active phase; (b) is during the residual stage; during (c), a second breaking wave entered the ROI and is seen as a second bright peak in the time series. Note that the time series of bright and dark relative area shows the evolution of the active and residual whitecap stages within the ROI, but does not provide rigorously extracted whitecap fraction; determination of whitecap fraction from IR images was not pursued in this study.

4. Results and Discussion

4.1. Breaking Events and Whitecap Lifetimes From IR Data

The examination of the IR images (section 3.2) identified 41 events captured simultaneously by the IR and visible cameras. As in Figure 6, visible images do not bear objective cues signifying the transition between whitecap stages. Meanwhile, the IR images provide evidence that the active and residual foams appear brighter and darker, respectively, than the ambient water surface. The midrange IR imaging can thus be used as a tool for clear, unambiguous separation of the whitecap lifetime stages.

Breaking event evolution, such as that shown in Figure 7, is exemplified with three more breaking waves in Figure 8. The patterns observed in Figures 7 and 8 are consistently repeated for all 41 cases. Specifically, the active whitecap stage (green) is characterized by rapid changes and is generally short lived within the ROI. In contrast, the residual whitecap stage (red) is typically prolonged and undulating. These undulations were reoccurring, but not universal, features of the residual whitecap stage. In about 30% of cases, the residual whitecap stage is depicted

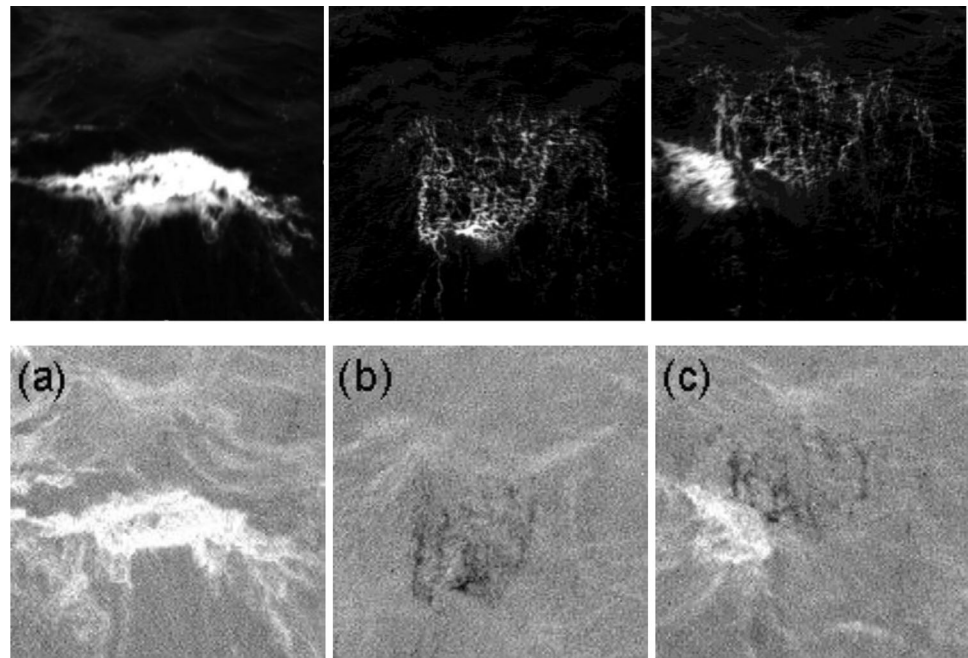


Figure 6. Breaking wave captured simultaneously in visible (top) and infrared (bottom). Each image pairs shows the wave evolution (a) 2 s, (b) 6.5 s, and (c) 8.5 s from the onset of the breaking event. Each image shows an area approximately 7 m × 7 m.

breaking event, which likely impacted this result. Under such circumstances, the active breaker propagated through the ROI, while residual foam remained relatively static and decayed within it. The wide variability of the active and residual stage durations τ_A and τ_B is likely caused by breaking at different scales as wind varied from 9 to 15 m s⁻¹ (Figure 3). However, no clear dependence of τ_A and τ_B on wind speed was observed. The water properties presumably influence τ_B more strongly than τ_A [Callaghan *et al.*, 2013], but these properties remained nearly constant during BREWEX (section 3.2).

Different explanations have been suggested about the appearance of active breaking crests and decaying foam as bright and dark patches in IR imagery. Jessup *et al.* [1997a] observed the breaking crests that were warmer than ambient by up to 0.1 K, but did not report dark, older foam. Marmorino and Smith [2005] supported the observation of breaking crest temperatures of up to 0.15 K warmer than ambient, but they also observed dark, residual foam. They offered that the cold foam was likely due to evaporative cooling of the water film of the topmost layer of foam bubbles.

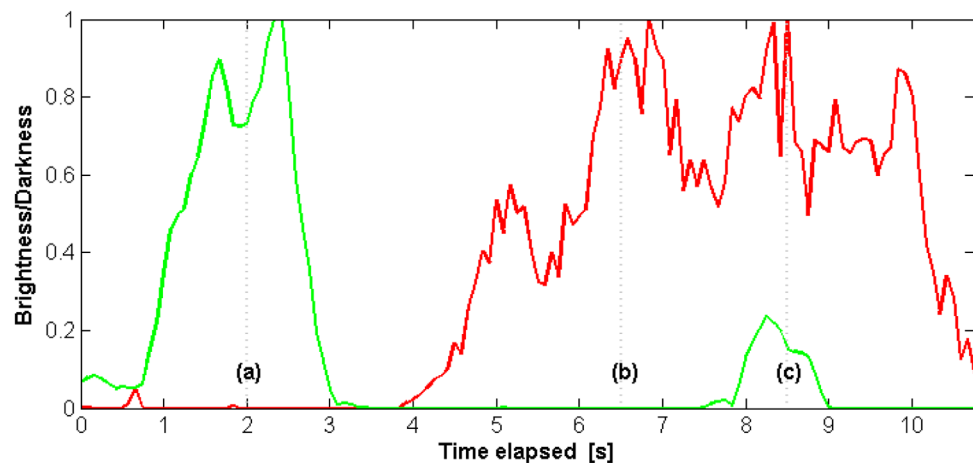


Figure 7. Infrared signal from the breaking event pictured in Figure 6. A pixel is considered bright (dark) if it is above (below) a threshold value. Brightness (green) and darkness (red) are normalized by their respective run maximums. Vertical lines (a), (b), and (c) correspond to timing of the images in Figure 6.

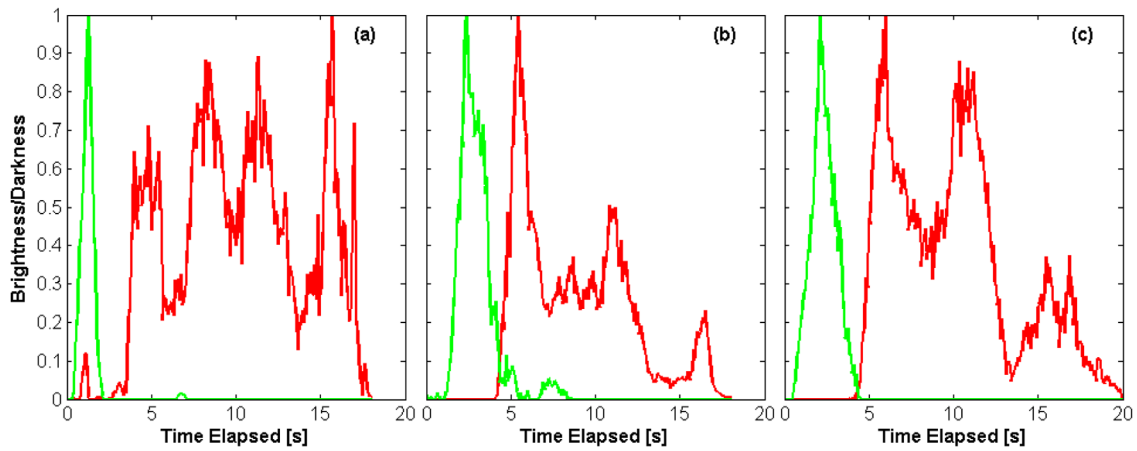


Figure 8. Examples of the temporal variations (evolutions) of three breaking waves captured with the IR imager. The active phase is shown in green and the residual phase in red.

4.2. Breaking Events From Radiometric Measurements

For the 41 breaking events captured with IR imagery, 24 were also captured by the microwave radiometer at 10 GHz. The times of the peaks of the active stage taken from the breaking event evolutions (e.g., Figures 7 and 8) were used to identify the corresponding changes in the radiometric time series. Figure 9 shows the

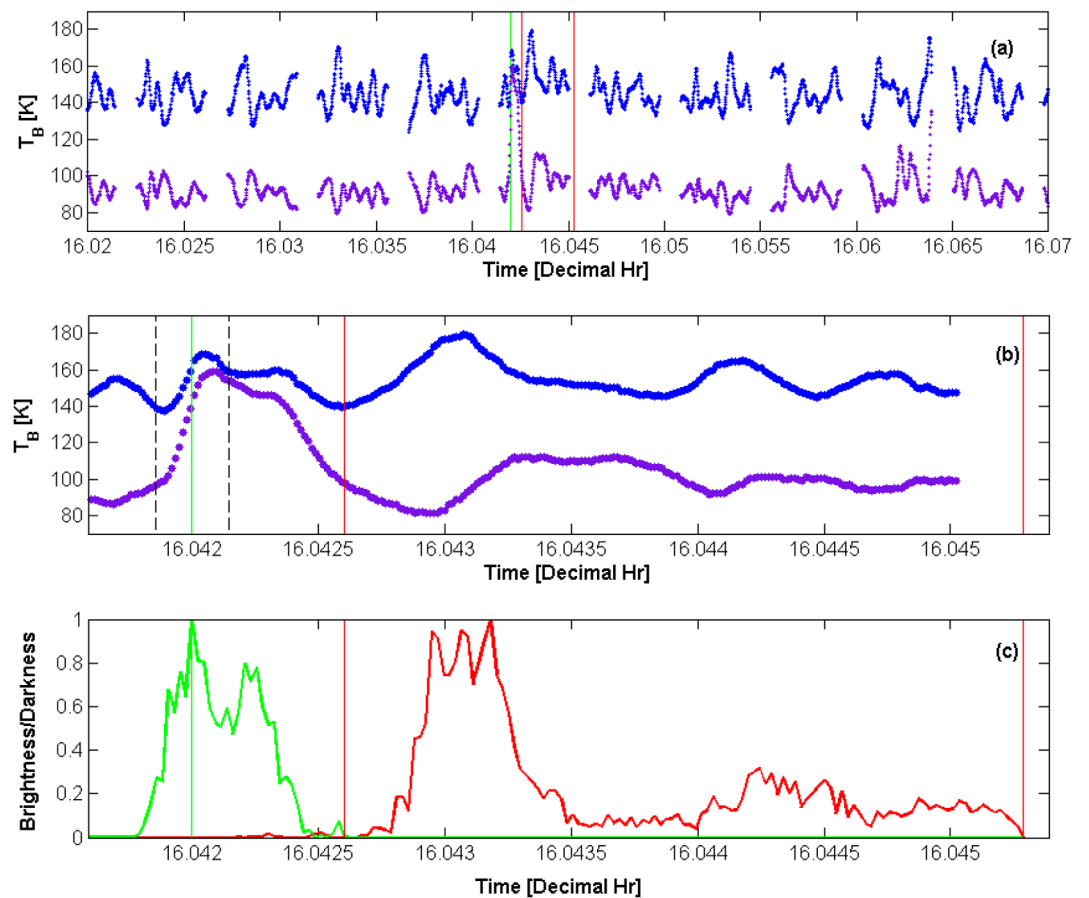


Figure 9. Breaking wave captured simultaneously at IR and microwave wavelengths: (a) time series of brightness temperatures T_B at horizontal (H, purple) and vertical (V, blue) polarizations aligned with the timing of active (green) and residual (red) stages of a breaking event captured in IR. (b) Zoom-in on the T_B for the specific breaking event. (c) Evolutions of active (green) and residual (red) whitecaps from the IR images. Vertical green line shows time of peak IR brightness during active phase. Dot-dash vertical lines show ± 0.52 s to account for uncertainty in IR time stamp.

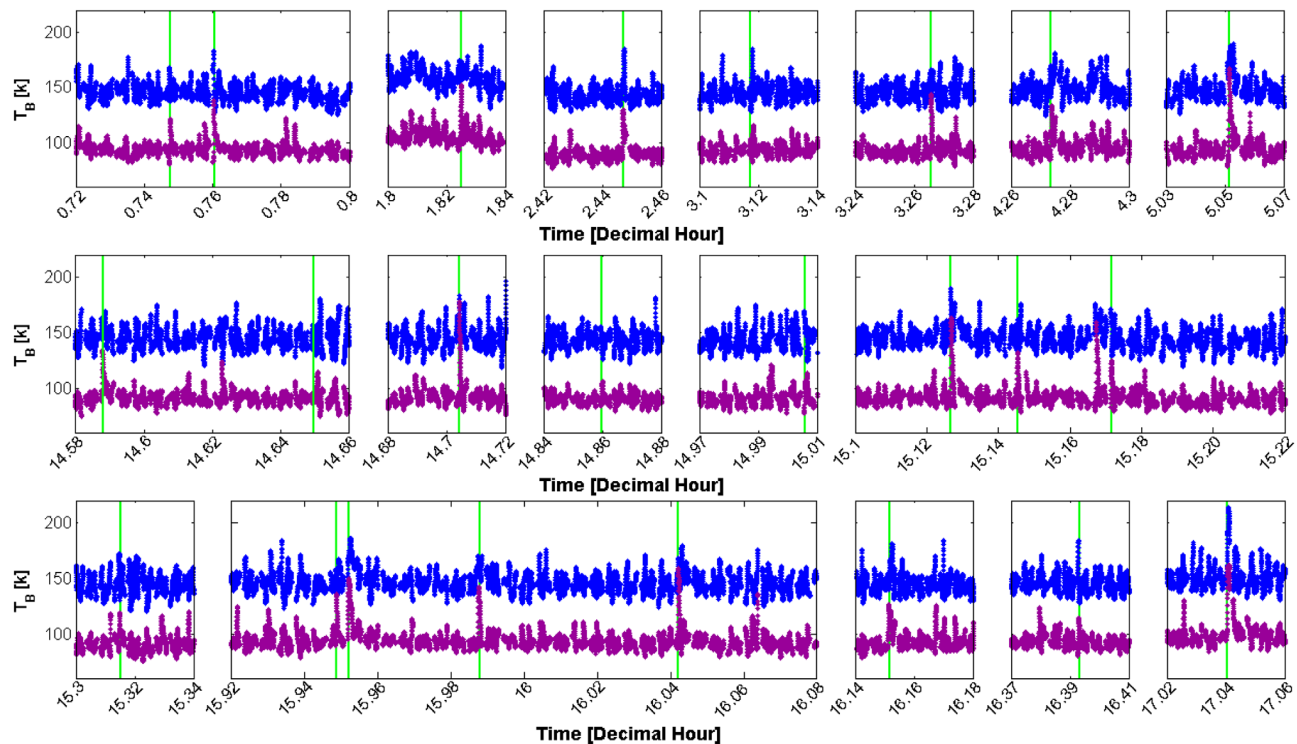


Figure 10. The time of all 24 breaking waves captured simultaneously in IR and microwave. Brightness temperature is for horizontal (purple) and vertical (blue) polarizations. Vertical green lines show time of peak IR brightness during the active phase of each breaking wave.

brightness temperature T_B time series (with breaks for internal calibration (section 2.1)) corresponding to the active and residual stages observed in the sequence of IR images for one breaking event. Figure 9a shows that using the time of the peak of the active whitecap stage from the IR images (green vertical line) we unambiguously identify a large T_B spike at H polarization (purple line). Figure 9b zooms in on the T_B data for this breaking event. The red vertical lines enclose the range of T_B values corresponding to the residual whitecap stage (red line in Figure 9c). We draw attention to three notable observations in Figure 9: (i) the relationship between the peaks in the IR and T_B data during the active whitecap stage; (ii) the relationship between the peaks in T_{BH} and T_{BV} data; and (iii) the concurrent variations of T_{BH} and T_{BV} values during the residual whitecap stage.

The peak of the active whitecap stage from IR images is associated with maxima in both T_{BH} and T_{BV} with an offset of 0.2919 s for T_{BH} (Figure 9b). This time misalignment is within the uncertainty of the IR time stamp σ_{IR} of 0.52 s (section 2.2). Similar temporal alignments were made for all 24 events captured simultaneously in the IR and radiometric data (Figure 10). The mean bias (with 1 standard deviation) between the times of IR and T_{BH} peaks is 0.3651 ± 0.3127 s. Time biases larger than the time stamp uncertainty σ_{IR} (from 0.627 to 0.9752 s) were observed in 30% of the cases. Examination of the IR and video images showed that such biases were caused by active whitecap stages occurring close to but not within the radiometer footprint (Figure 2b). The T_B peak at V polarization precedes the T_B peak at H by 0.105 s (Figure 9b). Such a shift is consistently observed in 90% of all cases (Figure 10) with a mean time shift of 0.36 ± 0.32 s between the T_{BH} and T_{BV} peaks.

In all cases, the T_B variations for the active and residual whitecap stages showed patterns like those in Figure 9b: concurrent T_{BH} and T_{BV} maxima for the active stage, and antiphase variations of T_{BH} and T_{BV} for the residual stage. The observation of simultaneous peaks in T_{BH} and T_{BV} is consistent with previous radiometric measurements at different frequencies and conditions [Smith, 1988; Padmanabhan et al., 2006]. The small time shift between the T_{BH} and T_{BV} peaks during τ_A has not been reported before, yet its repeatability in our data implies that it is a physical feature, not experimental artifact. The only case when a similar, but not well-defined pattern is apparent is for observations of breakers a 10 GHz (but not for higher frequencies) at azimuth angle of 180° [see Padmanabhan et al., 2006, Figure 16], a view similar to our downwind

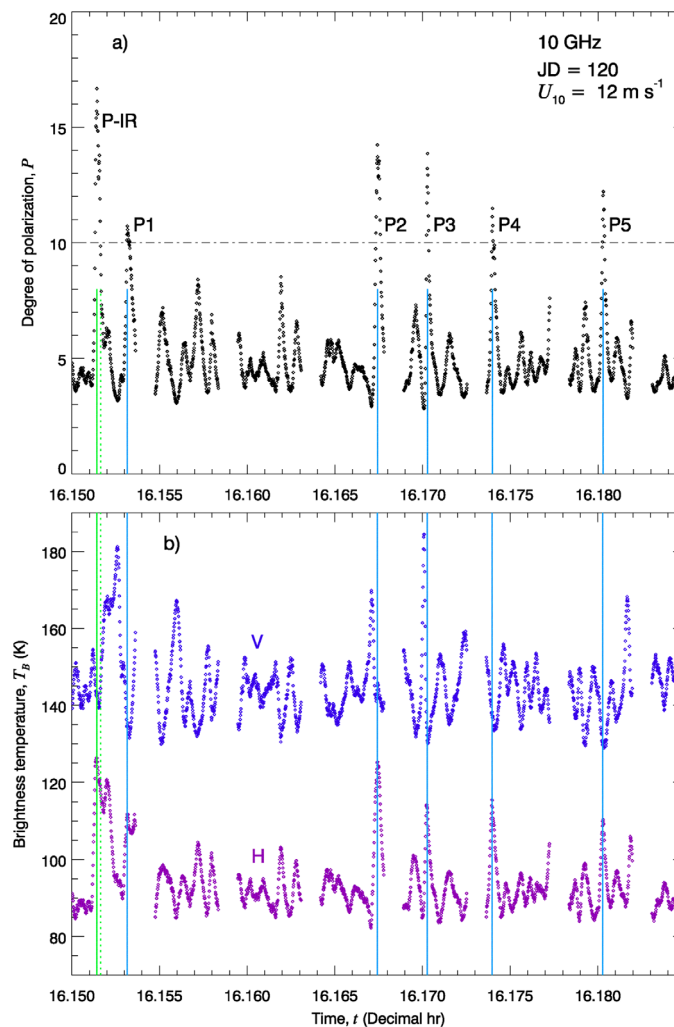


Figure 11. Zoom-in on the time series for the event in the range from 16.14 to 16.18 h in Figure 10: (a) the degree of polarization P (defined as the ratio of the sum and difference of brightness temperature at H and V polarizations (section 4.3)) and (b) T_{BH} (purple) and T_{BV} (blue) data. Vertical green lines are for the breaking event (named P_IR) identified from the IR images (as in Figure 10); dotted line for the timing from the IR data, solid line for the exact timing of the T_{BH} peak. Vertical blue lines are for the spikes in P above the arbitrary threshold of $P = 10$ (dash-dot line in Figure 11a), named P1 to P5.

at all other settings the same, i.e., both T_{BH} and T_{BV} increasing for warmer seawater or decreasing for cooler seawater. Therefore, thermal variations cannot be the cause for the antiphase variations. The most probable reason for opposite variations of T_{BH} and T_{BV} is from variations of the incidence angle [e.g., Padmanabhan *et al.*, 2006, Figures 5 and 6]. The steepness of a water wave changes significantly during the breaking process [Bonmarin, 1989]. At fixed incidence angle on FLIP (section 2.1), this yields variations of the incidence angle under which the radiometer observes the surface. Our IR data (Figures 7 and 8) show that the time intervals of 7–12 s between the peaks of the active whitecaps and (at least) some of the peaks of the residual whitecaps are comparable to the swell periods (section 2.3). This implies that the peaks during τ_A and τ_B are related to the phase of the wave (crest or trough) and thus lends support to the suggestion that variations of the incidence angle yield the antiphase pattern during τ_B . Perhaps this could have been verified and further studied if we could correlate the records of our pressure sensor and the T_B time series. However, the physical distance between the radiometer FOV (from the port boom) and the point of pressure sensor submergence (from the starboard boom) preclude such correlation for the individual breaking events considered here.

Overall, our result in Figure 9b suggests that the thermal variation, together with depolarization due to scattering within the foam (section 1), is the dominant process during the active whitecap stage that forms the

observations. This is a hint that different azimuthal dependences for the H and V polarizations, especially at a frequency with thicker skin depth like that for 10 GHz [Anguelova and Gaiser, 2011], might cause the consistent shift between the T_{BH} and T_{BV} peaks during τ_A . However, our data at one azimuth angle and one frequency do not provide sufficient information to further study and understand this observation. More diverse T_B data set of breaking events at different frequencies and different azimuth angles would be helpful to verify and explain this observation.

The antiphase variations of T_{BH} and T_{BV} during the residual stage are not clearly observed by Smith [1988] and Padmanabhan *et al.* [2006]. Rather, previous observations show more in-phase T_B variations at all frequencies and different whitecap stages. How can such a curious antiphase pattern during the residual stage be explained? Because variations of T_B are associated with the physical temperature of the seawater, the cooling of the decaying foam could be one possible reason. However, thermal variations (heating or cooling) of the seawater cause the same (in-phase) variations of T_{BH} and T_{BV}

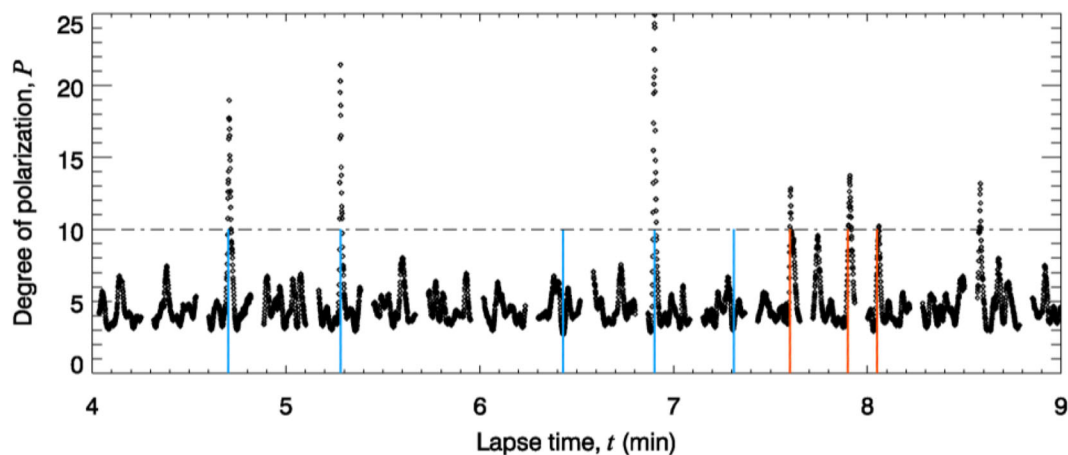


Figure 12. Time series of the degree of polarization P corresponding to the time series in Figure 5a. The red and blue lines are as in Figure 5a.

T_B response. During the residual whitecap stage, it is likely that T_B responds more strongly to the variations of the wave steepness than to the cooling of the surface.

4.3. Signatures of Whitecap Lifetime Stages in Microwave Radiometric Measurements

The unique whitecap signature at mid-IR wavelengths allowed us to unambiguously determine breaking wave events and their lifetime stages in time series of radiometric measurements of brightness temperature T_B at 10 GHz (section 4.2). In this section, we look into devising a means to uniquely recognize the signature of active and residual whitecaps in the T_B time series without a priori information from IR images. We use the IR imagery and the accompanying video data to verify how well our approach is performing.

We start by modifying the T_B time series so that the simultaneous T_B maxima at H and V polarizations seen in Figures 9 and 10 are clearly identified. Figure 5b shows three possible modifications of the T_B data (section 3.1). Trials of more combinations showed that the ratio of the sum and difference of T_{BV} and T_{BH} , i.e., $P = (T_{BV} + T_{BH}) / (T_{BV} - T_{BH})$, works best; we refer to P as the degree of polarization. Figure 11a shows time series of P for the breaking event identified from the IR imagery in the period 16.14–16.18 h (Figure 10); Figure 11b shows the corresponding T_{BH} and T_{BV} data. The time of the peak of the active whitecap obtained from the IR data and the exact time of the corresponding T_{BH} peak are marked (dotted and solid green vertical lines, respectively). The figure demonstrates that the simultaneous T_B peaks (with T_{BV} slightly preceding T_{BH} , plot b) emerge as a spike in P (referred to as P-IR in Figure 11a). All peaks of the active whitecap stage identified from the IR imagery (green lines in Figure 10) are seen as such spikes in time series of P . Though present, such P-IR spikes were not prominent in five cases. For these five cases, the bias between IR and T_B timing or the temporal shift between T_{BH} and T_{BV} peaks were larger than $\sigma_{IR} = 0.52$ s because the active phase peak did not occur within the radiometer footprint (section 4.2). Overall, we surmise that the degree of polarization P is a suitable quantity to determine the presence of active whitecaps.

To verify the reliability of this criterion developed using the IR data, we proceeded to identify breaking events and presence of active whitecaps solely from time series of the degree of polarization P . Figure 11a shows that, beside the breaking event identified from the IR imagery (P-IR), several more spikes appear in the P time series, which could be possible signatures of active whitecaps. Imposing an arbitrary threshold of $P = 10$ (dash-dot line in Figure 11a), five spikes were considered (marked with blue vertical lines and referred to as P1 to P5). Figure 11b shows that these five P spikes are associated with simultaneous T_{BH} and T_{BV} peaks in some cases (e.g., events P2 and P3), while the other cases have peaks either at H or at V polarization. As in Figure 5a, this ambiguity precludes prediction of active whitecaps with certainty; however, we now can use IR imagery to resolve this uncertainty.

Using the times of each of these five spikes, we searched the IR imagery to verify if they are indeed signatures of whitecaps. The search showed breaking events for spikes P2, P3, and P4. Bright and dark pixels were evident for these events, though they were much fainter compared to the clear cut cases summarized in Figure 10. Spikes P1 and P5 in Figure 11a were not clearly associated with breaking events in the IR imagery. Figure 11b shows that these are cases in which T_{BV} peaks are missing. These results establish firmly that either a spike in P or a tandem of a T_{BH} peak and a close by T_{BV} peak represent a whitecap signature.

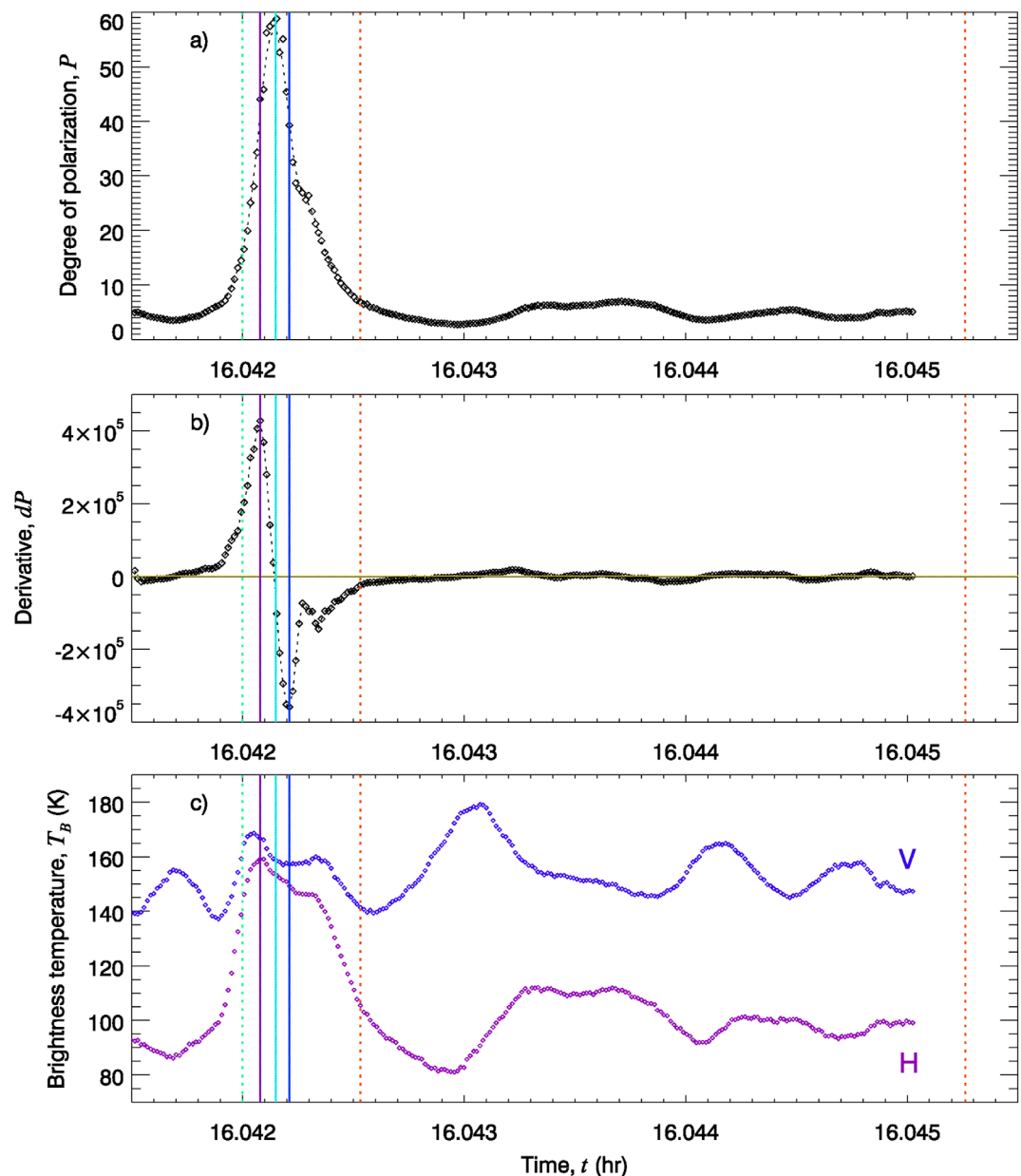


Figure 13. (a) Time series of the degree of polarization P for the event in Figure 9. (b) First derivative of P , denoted dP . (c) Replot of T_{BH} (purple) and T_{BV} (blue) data in Figure 9. Dotted lines are from the IR data analysis: green line for the peak of the active whitecap; red lines for the duration of the residual whitecap. Solid lines denote the maximum (purple), zero-crossing (cyan), and minimum (blue) of dP .

To verify the repeatability of these results, we performed the same procedure for the cases in Figure 5a marked with red and blue lines. All spikes but one in the respective P time series (Figure 12) yielded breaking events and whitecaps in the IR imagery. The one case which did not identify a whitecap using the degree of polarization P (at ~ 6.4 min in Figure 12) has a strong peak in T_{BV} but no peak in T_{BH} (Figure 5a). This suggests that the criterion for identifying the active part of a whitecap can be strengthened by requiring spikes in both T_{BH} and P .

To find a criterion determining the transition from active to residual lifetime stage of the whitecaps, we considered the information provided by the first derivative of the spikes in the P time series; we illustrate this in Figure 13. Figure 13a shows the time series of the degree of polarization P for the event shown in Figure 9 (replotted in Figure 13c). The peak of the active whitecap stage and the duration of the residual whitecap stage obtained from the IR images are shown for guidance with vertical dotted lines (color convention as in Figure 9). Figure 13b shows the derivative dP of the P spike in Figure 13a. The times of the maximum, the

zero-crossing and the minimum of dP (denoted dP_{max} , dP_0 , and dP_{min} , respectively) are taken from this graph and overlaid on the P and T_B time series in plots a and c. We see from Figure 13 that using the times of dP_{max} and dP_0 is the most rigorous way to locate the peaks of T_{BH} and P and thus identify the presence and time of active whitecaps. The time of dP_{min} marks the start of transition from active to residual whitecap stage. This is the point from which the in-phase variations of T_{BH} and T_{BV} start to deviate and gradually attain antiphase pattern within the residual stage. It is anticipated that using whitecap signatures in T_B and P time series at more frequencies, instead of only one as in the case presented here, would help to develop even more specific and reliable criteria for detecting and separating active and residual whitecaps with radiometric measurements.

Our analysis here involves clearly identified individual breaking events. The careful examination and choice of the IR images (section 3.2) aimed at extracting unambiguous cases which show convincingly the clear separation of whitecap lifetime stages in IR, and then in T_B data. Therefore, we do not provide an extensive study of the variations caused by the presence of multiple wave trains and breaking events within the FOVs of the IR camera and the radiometer. Undoubtedly, such occasions exist. Figures 6 and 7 show one example of mixing up active and residual whitecaps within the same FOV. The results in section 4.2 quantify some of the variations caused by breaking events occurring close, but not within, the radiometer FOV. The methodology outlined here is thus suitable for individual breaking events and whitecaps. Such analysis would be useful when radiometric measurements at high spatial resolution are available, e.g., from radiometers deployed on low flying airplane.

However, T_B and P time series would not be as informative as shown here when the radiometer FOV encompasses multiple wave trains and numerous whitecaps yielding concurrent existence of many stage A and stage B plumes with random times since inception and decay. This is a scene that would be observed either at very high wind speeds when most aircrafts will not operate close enough to the ocean surface (due to salt ingestion by the engines) to provide a footprint small enough to observe individual whitecaps or by satellite-based radiometers. To extract the signature of an ensemble of active or residual whitecaps, we could build on the insights gained here but use statistical analysis of T_B and P time series in order to generalize the methodology. Such statistical analysis is not trivial and calls for extensive future work.

5. Conclusions

Whitecaps formed by wave breaking and air entrainment are dynamic features on the ocean surface which evolve quickly and thus have markedly different properties in different lifetime stages. Active whitecaps accompany the turbulent mixing in the moment of wave breaking. In contrast, residual whitecaps are almost motionless foam patches left behind the breaking wave. The relative contributions of active and residual whitecaps to air-sea interaction processes differ. Therefore, to properly parameterize modifications of momentum, heat, and mass transfers across the air-sea interface in presence of breaking waves, it is desirable to separately quantify the fraction of the ocean surface covered by active and residual whitecaps.

Because active and residual whitecaps in photographic and radiometric observations exhibit small, subtle changes of image intensity and surface emissivity, respectively, their separation at visible wavelengths or microwave frequencies is highly uncertain. Infrared (IR) imagery at 3–5 μm provides clear separation of the whitecap lifetime stages because active and residual whitecaps are represented with opposite signatures, i.e., bright and dark pixels (section 1). This study describes observations from multi-instrumental field campaign on FLIP (section 2 and Figures 1–3) and data analysis that demonstrates the application of the specific IR signature of whitecaps to facilitated identification of active and residual whitecap stages in radiometric measurements (section 3 and Figures 4 and 5). The major results (section 4) and conclusions of this study are:

1. Forty-one breaking events captured simultaneously in video and IR imagery provide experimental evidence to previous observations [Marmorino and Smith, 2005] that the IR signature of breaking crests (active whitecaps) is high temperature (bright pixels) and decaying foam (residual whitecaps) is low temperature (dark pixels) (Figure 6).
2. Temporal variations (evolutions) of active and residual whitecap stages, extracted from IR imagery, are presented for the first time (Figures 7 and 8). The duration of active whitecaps τ_A ranges from 0.4 to 5 s for wind speeds from 9 to 15 m s^{-1} with a rapid growth of its spatial extent to a maximum value for a period of up to 1 s. The duration of residual whitecaps τ_B is from 3 to 30 s with two and more peaks over its prolonged lifetime. These whitecap lifetime stages differ by a factor of 1 to 10. No clear dependence of τ_A and τ_B on wind speed was observed.

3. Simultaneous capture of 24 breaking events in both IR imagery and microwave brightness temperature T_B allows unambiguous identification of whitecap signature in T_B time series. Within the uncertainty of the IR time stamp, the peaks of the active whitecaps in IR images correspond to pairs of peaks in T_B at horizontal and vertical (H and V) polarizations in 70% of the cases (Figures 9 and 10). The T_{BV} peak precedes the T_{BH} peak in 90% of the cases with an average value of 0.36 ± 0.32 s.
4. In all cases, T_{BH} and T_{BV} vary in-phase during the active whitecap stage and in antiphase during the residual whitecap stage (Figure 9). The in-phase variations during τ_A are explained by T_B response to warmer water, higher emissivity due to optimal impedance matching of foam with high void fraction, and radiation depolarization. During τ_B , the antiphase variations are caused by different responses of T_{BH} and T_{BV} to wave steepness.
5. A methodology to distinguish the signature of active and residual whitecaps in radiometric time series without a priori IR information has been developed (section 4.3). The degree of polarization $P = (T_{BV} + T_{BH}) / (T_{BV} - T_{BH})$ is a suitable quantity to capture breaking events as prominent spikes (Figures 11 and 12). The utility of spikes in time series of P has been verified with identification of breaking events in the corresponding IR and video images.
6. Stringent requirement for detection of active whitecap is observation of peaks in times series of both P and T_{BH} . The most rigorous way to determine the peak and timing of active whitecap is to use the first derivative of P (Figure 13). The maximum of dP pin-points the T_{BH} peak, while the zero-crossing of dP determine the P peak. The transition from active to residual whitecaps starts at the minimum of dP .
7. The methodology for identifying the signatures of active and residual whitecaps in brightness temperature T_B time series is suitable for individual whitecaps which can be observed from ship or low-flying airplane. Application of the IR- T_B information described here for satellite-based radiometric measurements requires more data and statistical analysis.

Acknowledgments

This work was sponsored by the Office of Naval Research (ONR), NRL Program element 61153N WUs 4500. This research was performed while Henry Potter held an NRC Research Associateship award at The Naval Research Laboratory. We highly appreciate the funding support for our use of FLIP by Robert Schnoor via the Naval Research Facilities Program at ONR and by Joan Gardner and Edward Franchi via the NRL Platform Support Program. Captain William Gaines, FLIP program manager at Marine Physics Laboratory (MPL) at Scripps Institution of Oceanography, was indispensable in organizing the field campaign. We appreciate Tom Golfinos, Officer-in-Charge for FLIP, and crew members Johnny, Dave, Frank, and Jerry for their hard work, endurance, and camaraderie. We would also like to thank George Trekas and his colleagues at the MPL Machine Shop for their expertise and skills in devising the instrument deployment on the FLIP booms. We would also like to thank all the other participants in the BREWEX experiment; while not explicitly part of this work, their help during the preparation and cruise was invaluable. We also thank the two anonymous reviewers for their careful reviews and valuable suggestions which strengthened the paper. Data used in this manuscript are available upon request, please contact the corresponding author.

References

- Anguelova, M. D., and P. W. Gaiser (2011), Skin depth at microwave frequencies of sea foam layers with vertical profile of void fraction, *J. Geophys. Res.*, *116*, C11002, doi:10.1029/2011JC007372.
- Anguelova, M. D., and P. W. Gaiser (2012), Dielectric and radiative properties of sea foam at microwave frequencies: Conceptual understanding of foam emissivity, *Remote Sens.*, *4*, 1162–1189, doi:10.3390/rs4051162.
- Anguelova, M. D., and P. W. Gaiser (2013), Microwave emissivity of sea foam layers with vertically inhomogeneous dielectric properties, *Remote Sens. Environ.*, *139*, 81–96, doi:10.1016/j.rse.2013.07.017.
- Anguelova, M. D., and P. A. Hwang (2012), Whitecap fraction of actively breaking waves: Toward a database applicable for dynamic processes in the upper ocean, in *18th Air-Sea Interaction Conference*, Am. Meteorol. Soc., Boston, Mass. [Available at <https://ams.confex.com/ams/20BLT18AirSea/webprogram/Manuscript/Paper209178/separateWA.pdf>]
- Anguelova, M. D., and P. Huq (2012), Characteristics of bubble clouds at various wind speeds, *J. Geophys. Res.*, *117*, C03036, doi:10.1029/2011JC007442.
- Anguelova, M. D., and F. Webster (2006), Whitecap coverage from satellite measurements: A first step toward modeling the variability of oceanic whitecaps, *J. Geophys. Res.*, *111*, C03017, doi:10.1029/2005JC003158.
- Anguelova, M. D., M. Bettenhausen, and P. Gaiser (2006), Passive remote sensing of sea foam using physically-based models, in *IEEE International Conference on Geoscience and Remote Sensing Symposium, IGARSS2006*, pp. 3676–3679, IEEE, Denver, Colo. doi:10.1109/IGARSS.2006.942.
- Anguelova, M. D., P. W. Gaiser, and V. Raizer (2009), Foam emissivity models for microwave observations of oceans from space, in *IEEE International Geoscience and Remote Sensing Symposium, IGARSS2009*, vol. 2, pp. II-274–II-277, IEEE, Cape Town, South Africa. doi:10.1109/IGARSS.2009.5418061.
- Anguelova, M. D., M. Bettenhausen, W. Johnston, and P. Gaiser (2010), First extensive whitecap database and its use to study whitecap fraction variability, in *17th Air-Sea Interaction Conference*, Am. Meteorol. Soc., Annapolis, Md. [Available at <https://ams.confex.com/ams/pdffpapers/174036.pdf>]
- Anguelova, M. D., D. J. Dowgiallo, G. B. Smith, S. L. Means, I. B. Savelyev, G. M. Frick, C. M. Snow, J. A. Schindall, and J. P. Bobak (2013), Remote sensing signatures of breaking waves from multi-instrument field experiment on FLIP, in *The Annual NRL Review*, pp. 214–216, Naval Research Laboratory, Washington, D. C. [Available at http://www.nrl.navy.mil/content_images/2013_NRL_Review_cleansed.pdf]
- Bobak, J. P., D. J. Dowgiallo, N. R. McGlothlin, K. M. St Germain (2001), "APMIR: airborne polarimetric microwave imaging radiometer," in *Geoscience and Remote Sensing Symposium, IGARSS '01. IEEE 2001 International*, vol. 1, pp. 505–507, doi:10.1109/IGARSS.2001.976204.
- Bobak, J. P., W. E. Asher, D. J. Dowgiallo, and M. D. Anguelova (2011), Aerial radiometric and video measurements of whitecap coverage, *IEEE Trans. Geosci. Remote Sens.*, *49*, 2183–2193, doi:10.1109/TGRS.2010.2103565.
- Bonmarin, P. (1989), Geometric properties of deep-water breaking waves, *J. Fluid Mech.*, *209*, 405–433, doi:10.1017/S0022112089003162.
- Callaghan, A. H., and M. White (2009), Automated processing of sea surface images for the determination of whitecap coverage, *J. Atmos. Oceanic Technol.*, *26*, 383–394, doi:10.1175/2008JTECH0634.1.
- Callaghan, A. H., G. B. Deane, M. D. Stokes, and B. Ward (2012), Observed variation in the decay time of oceanic whitecap foam, *J. Geophys. Res.*, *117*, C09015, doi:10.1029/2012JC008147.
- Callaghan, A. H., G. B. Deane, and M. Dale Stokes (2013), Two regimes of laboratory whitecap foam decay: Bubble-plume controlled and surfactant stabilized, *J. Phys. Oceanogr.*, *43*, 1114–1126, doi:10.1175/JPO-D-12-0148.1.
- Carini, R. J., C. C. Chickadel, A. T. Jessup, and J. Thomson (2015), Estimating wave energy dissipation in the surf zone using thermal infrared imagery, *J. Geophys. Res. Oceans*, *120*, 3937–3957, doi:10.1002/2014JC010561.

- Catalán, P. A., M. C. Haller, R. A. Holman, and W. J. Plant (2011), Optical and microwave detection of wave breaking in the surf zone, *IEEE Trans. Geosci. Remote Sens.*, *49*, 1879–1893, doi:10.1109/TGRS.2010.2095864.
- de Leeuw, G., E. Andreas, M. D. Anguelova, C. Fairall, E. Lewis, C. O'Dowd, M. Schulz, and S. Schwartz (2011), Production flux of sea-spray aerosol, *Rev. Geophys.*, *49*, RG2001, doi:10.1029/2010RG000349.
- Frouin, R., M. Schwindling, and P.-Y. Deschamps (1996), Spectral reflectance of sea foam in the visible and near-infrared: In situ measurements and remote sensing implications, *J. Geophys. Res.*, *101*, 14,361–14,371.
- Gaiser, P. W., et al. (2004), "The WindSat spaceborne polarimetric microwave radiometer: sensor description and early orbit performance," in *Geoscience and Remote Sensing*, IEEE Transactions on, vol. 42(11), 2347–2361. doi:10.1109/TGRS.2004.836867.
- Gemmrich, J. R., M. L. Banner, and C. Garrett (2008), Spectrally resolved energy dissipation rate and momentum flux of breaking waves, *J. Phys. Oceanogr.*, *38*, 1296–1312.
- Hanson, J. L., and O. M. Phillips (1999), Wind sea growth and dissipation in the open ocean, *J. Phys. Oceanogr.*, *29*, 1633–1648.
- Hollinger, J. (1971), Passive microwave measurements of sea surface roughness, *IEEE Trans. Geosci. Electron.*, *9*, 165–169.
- Hwang, P. A., I. B. Savelyev, and M. D. Anguelova (2015), Wave breaking efficiency of bubble-related air-sea interaction processes, paper presented at the 7th International Symposium on Gas Transfer at Water Surfaces, University of Washington, Seattle, Wash.
- Jessup, A. T., W. C. Keller, and W. K. Melville (1990), Measurements of sea spikes in microwave backscatter at moderate incidence, *J. Geophys. Res.*, *95*, 9679–9688.
- Jessup, A. T., C. J. Zappa, M. R. Loewen, and V. Hesany (1997a), Infrared remote sensing of breaking waves, *Nature*, *385*, 52–55.
- Jessup, A. T., C. J. Zappa, and H. Yeh (1997b), Defining and quantifying microscale wave breaking with infrared imagery, *J. Geophys. Res.*, *102*, 23,145–23,153.
- Kleiss, J. M., and W. K. Melville (2010), Observations of wave breaking kinematics in fetch-limited seas, *J. Phys. Oceanogr.*, *40*, 2575–2604, doi:10.1175/2010JPO4383.1.
- Kleiss, J. M., and W. K. Melville (2011), The analysis of sea surface imagery for whitecap kinematics, *J. Atmos. Oceanic Technol.*, *28*, 219–243, doi:10.1175/2010JTECHO744.1.
- Koepke, P. (1984), Effective reflectance of oceanic whitecaps, *Appl. Opt.*, *23*, 1816–1824.
- Koepke, P. (1986), Remote sensing signature of whitecaps, in *Oceanic Whitecaps and Their Role in Air-Sea Exchange Processes*, edited by E. C. Monahan and G. M. Niocaill, pp. 251–260, D. Reidel, Dordrecht, Netherlands.
- Kokhanovsky, A. A. (2004), Spectral reflectance of whitecaps, *J. Geophys. Res.*, *109*, C05021, doi:10.1029/2003JC002177.
- Marmorino, G. O., and G. B. Smith (2005), Bright and dark ocean whitecaps observed in the infrared, *Geophys. Res. Lett.*, *32*, L11604, doi:10.1029/2005GL023176.
- Mironov, A. S., and V. A. Dulov (2008), Detection of wave breaking using sea surface video records, *Meas. Sci. Technol.*, *19*, 015405, doi:10.1088/0957-0233/19/1/015405.
- Monahan, E. C., and I. G. O'Muircheartaigh (1986), Whitecaps and the passive remote-sensing of the ocean surface, *Int. J. Remote Sens.*, *7*, 627–642.
- Monahan, E. C., and D. K. Woolf (1989), Comments on "Variations of whitecap coverage with wind stress and water temperature," *J. Phys. Oceanogr.*, *19*, 706–709.
- Monahan, E. C., K. L. Davidson, and D. E. Spiel (1982), Whitecap aerosol productivity deduced from simulation tank measurements, *J. Geophys. Res.*, *87*, 8898–8904.
- Niclòs, R., V. Caselles, E. Valor, and C. Coll (2007), Foam effect on the sea surface emissivity in the 8–14 μm region, *J. Geophys. Res.*, *112*, C12020, doi:10.1029/2007JC004521.
- Nordberg, W., J. Conaway, D. B. Ross, and T. Wilheit (1971), Measurements of microwave emission from a foam-covered, wind-driven sea, *J. Atmos. Sci.*, *28*(3), 429–435.
- Padmanabhan, S., S. C. Reising, W. E. Asher, L. A. Rose, and P. W. Gaiser (2006), Effects of foam on ocean surface microwave emission inferred from radiometric observations of reproducible breaking waves, *IEEE Trans. Geosci. Remote Sens.*, *44*, 569–583.
- Page, A. C., M. A. Bourassa, and M. D. Anguelova (2015), Comparing in situ and satellite-based observations of oceanic whitecaps, *J. Geophys. Res. Oceans*, *120*, 2826–2843, doi:10.1002/2014JC010328.
- Phillips, O. M. (1985), Spectral and statistical properties of the equilibrium range in wind-generated gravity-waves, *J. Fluid Mech.*, *156*, 505–531.
- Rogers, W. E., A. V. Babanin, and D. W. Wang (2012), Observation-consistent input and whitecapping dissipation in a model for wind-generated surface waves: Description and simple calculations, *J. Atmos. Oceanic Technol.*, *29*, 1329–1346, doi:10.1175/JTECH-D-11-00092.1.
- Rose, L. A., W. E. Asher, S. C. Reising, P. W. Gaiser, K. M. St. Germain, D. J. Dowgiallo, K. A. Horgan, G. Farquharson, and E. J. Knapp (2002), Radiometric measurements of the microwave emissivity of foam, *IEEE Trans. Geosci. Remote Sens.*, *40*, 2619–2625, doi:10.1109/TGRS.2002.807006.
- Salisbury, D. J., M. D. Anguelova, and I. M. Brooks (2013), On the variability of whitecap fraction using satellite-based observations, *J. Geophys. Res. Oceans*, *118*, 6201–6222, doi:10.1002/2013JC008797.
- Salisbury, D. J., M. D. Anguelova, and I. M. Brooks (2014), Global distribution and seasonal dependence of satellite-based whitecap fraction, *Geophys. Res. Lett.*, *41*, 1616–1623, doi:10.1002/2014GL059246.
- Savelyev, I. B., M. D. Anguelova, G. M. Frick, D. J. Dowgiallo, P. A. Hwang, P. F. Caffrey, and J. P. Bobak (2014), On direct passive microwave remote sensing of the sea spray aerosol production, *Atmos. Chem. Phys.*, *14*, 11,611–11,631, doi:10.5194/acp-14-11611-2014.
- Scanlon, B., and B. Ward (2013), Oceanic wave breaking coverage separation techniques for active and maturing whitecaps, *Methods Oceanogr.*, *8*, 1–12.
- Smith, P. M. (1988), The emissivity of sea foam at 19 and 37 GHz, *IEEE Trans. Geosci. Remote Sens.*, *26*(5), 541–547.
- Sugihara, Y., H. Tsumori, T. Ohga, H. Yoshioka, and S. Serizawa (2007), Variation of whitecap coverage with wave-field conditions, *J. Mar. Syst.*, *66*, 47–60.
- Sutherland, P., and W. K. Melville (2013), Field measurements and scaling of ocean surface wave-breaking statistics, *Geophys. Res. Lett.*, *40*, 3074–3079, doi:10.1002/grl.5058.
- Sutherland, P., and W. K. Melville (2015), Field measurements of surface and near-surface turbulence in the presence of breaking waves, *J. Phys. Oceanogr.*, *45*, 943–965, doi:10.1175/JPO-D-14-0133.1.
- Wang, Q., E. C. Monahan, W. E. Asher, and P. M. Smith (1995), Correlations of whitecap coverage and gas transfer velocity with microwave brightness temperature for plunging and spilling breaking waves, in *Air-Water Gas Transfer*, edited by B. Jähne and E. C. Monahan, pp. 217–225, AEON Verlag & Studio, Hanau, Germany.
- Whitlock, C. H., D. S. Bartlett, and E. A. Gurganus (1982), Sea foam reflectance and influence on optimum wavelength for remote sensing of ocean aerosols, *Geophys. Res. Lett.*, *9*, 719–722.
- Williams, G. F. (1971), Microwave emissivity measurements of bubbles and foam, *IEEE Trans. Geosci. Electron.*, *9*, 221–224.
- Zappa, C. J., W. E. Asher, and A. T. Jessup (2001), Microscale wave breaking and air-water gas transfer, *J. Geophys. Res.*, *106*, 9385–9391.